CHIN. PHYS. LETT. Vol. 38, No. 1 (2021) 017101

Large-Area Freestanding Weyl Semimetal WTe_2 Membranes

Yequan Chen(陈业全)[1], Ruxin Liu(刘汝新)[1], Yongda Chen(陈勇达)[1], Xiao Yuan(袁霄)[1], Jiai Ning(宁纪爱)[1], Chunchen Zhang(张纯臣)[2], Liming Chen(陈立明)[1], Peng Wang(王鹏)[2], Liang He(何亮)[1], Rong Zhang(张荣)[1], Yongbing Xu(徐永兵)[1*], and Xuefeng Wang(王学锋)[1*]

[1] *Jiangsu Provincial Key Laboratory of Advanced Photonic and Electronic Materials, School of Electronic Science and Engineering, and Collaborative Innovation Center of Advanced Microstructures, Nanjing University, Nanjing 210093, China*

[2] *College of Engineering and Applied Sciences, Nanjing University, Nanjing 210093, China*

(Received 2 November 2020; accepted 11 November 2020; published online 6 January 2021)

We report a universal transfer methodology for producing artificial heterostructures of large-area freestanding single-crystalline WTe_2 membranes on diverse target substrates. The transferred WTe_2 membranes exhibit a nondestructive structure with a carrier mobility comparable to that of as-grown films ($\sim$179–1055 $cm^2 \cdot V^{-1} \cdot s^{-1}$). Furthermore, the transferred membranes show distinct Shubnikov–de Haas quantum oscillations as well as weak localization/weak anti-localization. These results provide a new approach to the development of atom manufacturing and devices based on atomic-level, large-area topological quantum films.

DOI: 10.1088/0256-307X/38/1/017101

WTe_2, a typical type Ⅱ topological Weyl semimetal material with broken inversion symmetry and chiral Weyl fermions, possesses a layered structure and a distortion in the W chains along the *a* axis.[1] It has attracted widespread interest since 2014, owing to its exotic physical properties including huge unsaturated magnetoresistance (MR),[2,3] pressure-driven superconductivity,[4,5] quantum spin Hall effect,[6,7] ferroelectric switching in trilayer and bilayer structures,[8] nonlinear Hall[9] and nonlinear anomalous Hall effects.[10] Very recently, Song *et al.* achieved perfect contact between wafer-scale patterned WTe_2 films and monolayer MoS_2,[11] leading to the construction of high-performance field-effect transistors.

Atomic-level single-crystalline WTe_2 films with large surface areas, applied to various functional substrates (such as semiconductors, magnetic materials and flexible polymers), are of crucial importance, both for atom manufacturing and practical applications. To date, heterogeneous integration based on topological quantum materials has predominantly been implemented via mechanical exfoliation[12,13] and epitaxial growth.[14–17] However, mechanical exfoliation yields very limited sizes (generally less than 100 μm), rendering the fabrication of uniform devices difficult. Although epitaxial growth has been proposed with the aim of growing large-area WTe_2 thin films, the appropriate substrates and stringent growth conditions are key hurdles in terms of industrial applications.[6,11,18,19] Alternatively, nondestructive transfer technology, which has been executed in van der Waals films[20] and ultrathin oxide membranes,[21,22] provides a facile route to resolving the difficulty mentioned above. For example, freestanding membranes can be transferred onto any foreign substrate for a variety of prototype devices.[23,24] This approach has great potential for construction of artificial heterostructures based on transferred WTe_2 membranes. As a first step, this process requires the fabrication of large-area single-crystalline WTe_2 films, as realized in our earlier work.[25,26]

In this Letter, we demonstrate a reliable wet transfer technique to exfoliate large-area single-crystalline WTe_2 films, fabricated by pulsed laser deposition (PLD) on mica substrates. The exfoliated membranes can be freely transferred onto various target substrates, including silicon, sapphire, and poly-dimethylsiloxane (PDMS). The nondestructively transferred membranes demonstrate impressive properties, including weak localization (WL) and weak anti-localization (WAL) around zero fields, as well as the distinct Shubnikov–de Haas (SdH) oscillations. Based on a two-carrier model, the mobilities of 30 (100)-nm freestanding membranes are 920 (807) $cm^2 \cdot V^{-1} \cdot s^{-1}$ for holes and 179 (1055) $cm^2 \cdot V^{-1} \cdot s^{-1}$ for electrons, respectively, comparable to those of as-grown WTe_2 films. We anticipate that such a reliable transfer method could be extended to atom manufacturing and devices based on topological telluride films.

In our previous study,[25,26] single-crystalline WTe_2 films were prepared via PLD and subsequent post-annealing. Here, the high-quality WTe_2 films

Supported by the National Key R&D Program of China (Grant No. 2017YFA0206304), the National Natural Science Foundation of China (Grant Nos. 11874203, 61822403, U1732159, 11774160, and 61427812), and the Fundamental Research Funds for the Central Universities (Grant No. 021014380080).

*Corresponding author. Email: xfwang@nju.edu.cn; ybxu@nju.edu.cn

© 2021 Chinese Physical Society and IOP Publishing Ltd

were then exfoliated and transferred onto foreign substrates, similarly to $Bi_{2-x}Sb_xTe_{3-y}Se_y$ topological insulator ultrathin films.[27] The whole procedure is shown in Fig. 1(a). Firstly, the as-grown WTe_2/mica films were prepared by dipping into 2.38% tetramethylammonium hydroxide (ZX-238 type developer) aqueous solution for 10–20 s until the edges of the membranes began to peel away from the substrate. Secondly, the sample was carefully dipped into deionized water at an angle of ∼45° (between the sample and surface of the water). The completely peeled freestanding WTe_2 membranes, with thicknesses ranging from 5 to 100 nm were then floated on the surface of water. This step must be managed slowly and with great care, as the membranes are extremely delicate, even at a thickness of 100 nm. Thirdly, the target substrates (i.e., silicon and sapphire, as shown in the Supplementary Material) were used to pick up the freestanding membranes from the water. Finally, the transferred membranes underwent a one-hour annealing process at 100℃ in a vacuum chamber to remove residual water and air between the membranes and the substrates. Figures 1(b) and 1(c) show photographs of the freestanding WTe_2 membranes floating on water and stacked on PDMS, respectively. The stoichiometry of the transferred membranes was confirmed via x-ray photoelectron spectroscopy (XPS). Their surface morphology and thickness were examined by means of an atomic force microscope (AFM) system (Asylum Cypher). The crystalline structure was determined using a micro-Raman spectrometer (NT-MDT nanofinder-30), x-ray diffraction (XRD) (Rigaku Ultima Ⅲ), and a high-resolution transmission electron microscope (HRTEM). Their transport properties were measured using a Quantum Design physical property measurement system (PPMS-14 T). The typical experimental configuration for the transport measurement is shown in the Supplementary Material.

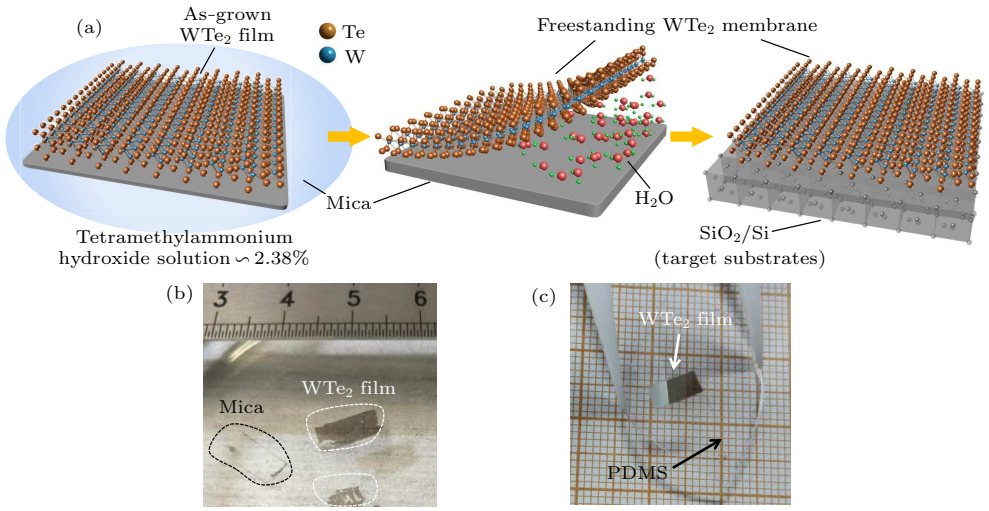

Fig. 1. Wet transfer methodology. (a) Diagrammatic sketch of wet transfer process: the WTe_2/mica films are dipped into a 2.38% tetramethylammonium hydroxide aqueous solution for 10–20 s; then the whole WTe_2 membrane is exfoliated from the mica utilizing the surface tension of the water; finally, the target substrates are used to pick up the freestanding WTe_2 membranes. (b) Photograph of freestanding WTe_2 membranes floating on the water. (c) Photograph of the transferred WTe_2 membrane on the PDMS.

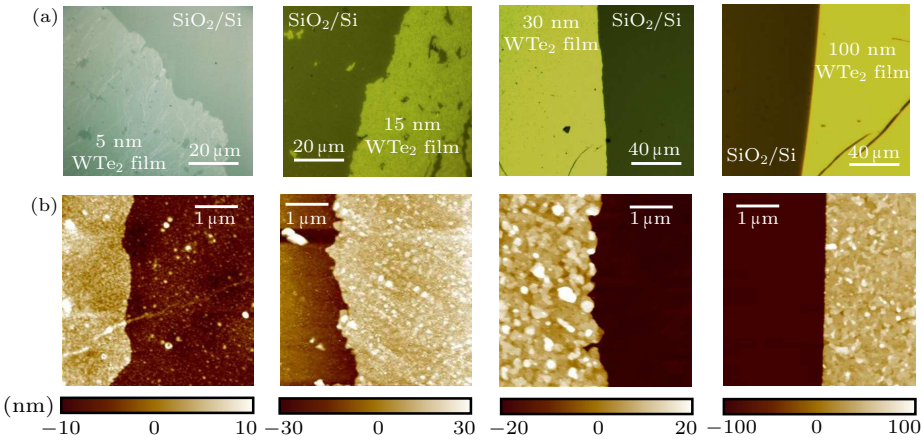

Fig. 2. Photographs (a) and AFM images (b) of transferred WTe_2 membranes with thicknesses of 5, 15, 30 and 100 nm, respectively.

Figure 2(a) comprises photographs of 5-, 15-, 30-, and 100-nm freestanding membranes transferred onto SiO_2/Si substrates. The corresponding AFM images are shown in Fig. 2(b). It is evident that the thin membranes (i.e., between 5-nm and 15-nm) have a few fissures and holes due to the unavoidable external force occurring during the transfer process. The AFM roughness of these membranes measures 5.8, 5.7, 18.2, and 21.3 nm, respectively, indicating that the thin membranes have a flat surface.

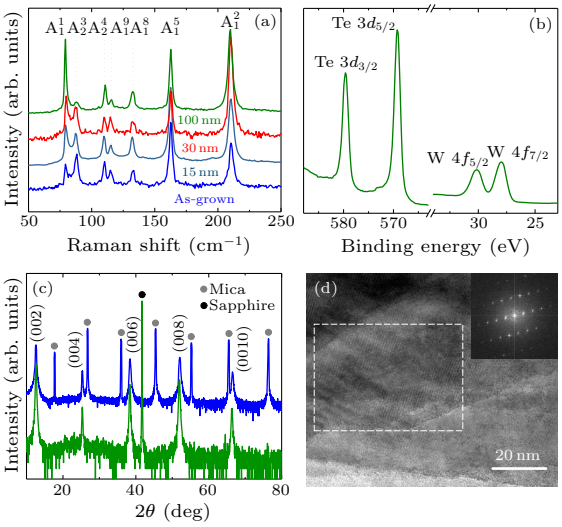

Fig. 3. Structural characterization of transferred WTe_2 membranes. (a) Raman spectra of the as-grown WTe_2 films and transferred membranes with thicknesses of 15, 30, and 100 nm, respectively. (b) XPS spectrum of the transferred WTe_2 membranes. (c) XRD patterns of the as-grown WTe_2 films and transferred membranes on sapphire. (d) HRTEM image of 100-nm transferred WTe_2 membrane. Inset shows the FFT pattern taken from the boxed area, demonstrating the membrane's single-crystalline structure.

Figure 3(a) shows the Raman spectra of the as-grown films and transferred freestanding membranes of different thicknesses. The Raman vibrational modes match those of T_d-phase WTe_2.[28] The XPS spectrum of a 100-nm transferred membrane is characterized by peaks of $3d_{5/2}$, $3d_{3/2}$ of Te and $4f_{5/2}$, $4f_{7/2}$ of W [Fig. 3(b)]. Quantitative analysis determines the stoichiometry of Te:W with an atomic ratio of 2.25. The typical XRD pattern for those membranes transferred onto sapphire reveals clear diffraction peaks, corresponding to the (002l) family of WTe_2 [see Fig. 3(c)]. The unmarked diffraction peaks can be ascribed to mica (as-grown) and the target substrate (transferred), respectively.[29] These results indicate that single-crystalline WTe_2 membranes can be realized via our transfer process. The HRTEM image and the corresponding fast Fourier transform (FFT) pattern further verify the single-orientation lattice structure and the single-crystalline nature of the 100-nm transferred membrane [see Fig. 3(d)]. These results demonstrate our ability to exfoliate WTe_2 films from mica and nondestructively transfer them to any foreign substrates.

Next, we measured the transport properties of the freestanding single-crystalline WTe_2 membranes via the standard six-probe method. The 30- and 100-nm transferred membranes were selected, so as to rule out the influence of the significant fissures and holes. Figure 4(a) shows their temperature-dependent resistance (R–T) curve. The residual resistivity ratios (RRRs), defined as $\mathrm{RRR} = \frac{\rho_{300\mathrm{K}}}{\rho_{2\mathrm{K}}}$, are 1.63 for the 30-nm as-grown film and 1.65 for the 30-nm transferred membrane, respectively. The temperature transition point at about 15 K [see the inset in Fig. 4(a)] is ascribed to the quantum interference effect.[30,31] Based on the localization theory and the insensitivity of electron–electron (e–e) interaction, the following equation is used to fit the R–T curve below 15 K:[32]

$$\rho = \rho_0 + \alpha T^5 - \beta T^{1/2} + \lambda \ln T, \tag{1}$$

where ρ_0 is the residual resistivity, αT^5 represents the inelastic scattering, $\beta T^{1/2}$ arises from e–e interaction,[33] and $\lambda \ln T$ is dominated by the WL effect. The excellent fitting results demonstrate the presence e–e interaction and WL effect in the transferred freestanding membranes (for further details, see the Supplementary Material). Figure 4(b) shows the field-dependent MR, where clear WL and WAL effects are evidenced only at 2 K. We convert the magnetoconductance from the enlarged low-field MR curves at 2 K, and observe the distinct difference between the two samples, as shown in Fig. 4(c). In order to better understand this difference, both curves are fitted via the Hikami–Larkin–Nagaoka (HLN) equation:[34]

$$\begin{aligned}&\Delta\sigma(B) - \Delta\sigma(0)\\ &= \frac{e^2}{\pi h}\Big\{\Psi\Big(\frac{1}{2} + \frac{B_\phi + B_{\mathrm{so}}}{B}\Big) + \frac{1}{2}\Psi\Big(\frac{1}{2} + \frac{B_\phi + 2B_{\mathrm{so}}}{B}\Big)\\ &\quad - \frac{1}{2}\Psi\Big(\frac{1}{2} + \frac{B_\phi}{B}\Big) - \ln\frac{B_\phi + B_{\mathrm{so}}}{B}\\ &\quad - \frac{1}{2}\ln\frac{B_\phi + 2B_{\mathrm{so}}}{B} + \frac{1}{2}\ln\frac{B_\phi}{B}\Big\},\end{aligned} \tag{2}$$

where $\Psi(\cdots)$ is the digamma function, B_ϕ and B_{so} are the characteristic fields for dephasing and spin-orbit interaction, respectively. The characteristic fields can also be written as $B_\phi = \hbar/4el_\phi^2$ and $B_{\mathrm{so}} = \hbar/4el_{\mathrm{so}}^2$, in which l_ϕ and l_{so} are the dephasing length and spin-orbit diffusion length, respectively. Here, B_ϕ for the freestanding membrane ($\sim$0.306) is larger than that of the as-grown film ($\sim$0.117), indicating a decrease in l_ϕ subsequent to transfer. The decreased dephasing length is partly due to the increased Te vacancies arising during the transfer process.[25] In our previous work, SdH quantum oscillations were observed in 100-nm as-grown WTe_2 films.[26] Remarkably, SdH quantum oscillations are still distinct in the 100-nm transferred WTe_2 membranes used in this work at

2 K [Fig. 4(d)]. From −14 to −3 T, the first two valleys (denoted by V_1 and V_2) and the first peak (denoted by P_1) of SdH oscillations are clearly observed. We note that the oscillation magnitude of the membranes shows a significant decrease, as compared to that of as-grown films. However, the FFT frequency is largely unchanged (approximately 179 T, see the Supplementary Material). This frequency reveals the cross-sectional area of the Fermi pocket (0.017 $Å^{-2}$) and the Fermi wave vector (0.074 $Å^{-1}$).[35,36]

Given that the Fermi surface is located at both conduction and valence bands, free electrons and holes simultaneously exist in WTe_2. In order to accurately define the mobility and carrier density of the transferred freestanding WTe_2 membranes, the conventional two-carrier model is used to fit the field-dependent resistivity, ρ_{xx}, and the Hall resistivity, ρ_{xy}, at 2 K[37] (see the Supplementary Material). In the 30-nm transferred membrane, the Hall mobilities of the holes and electrons are 920 and 179 $cm^2 \cdot V^{-1} \cdot s^{-1}$, while the corresponding carrier densities are 1.45×10^{19} and 1.14×10^{20} cm^{-3}, respectively. In the case of the 100-nm transferred membrane, the Hall mobilities of holes and electrons are 807.5 and 1055 $cm^2 \cdot V^{-1} \cdot s^{-1}$, while the corresponding carrier densities are 8.28×10^{19} and 1.65×10^{19} cm^{-3}, respectively. The unbalanced density of holes and electrons in the transferred membranes originate from the greater number of defects arising from the transfer process.[26] It is worth noting that the mobilities and the carrier densities of both 30- and 100-nm membranes are comparable to those of the as-grown WTe_2 films, confirming the reliability of our transfer method.

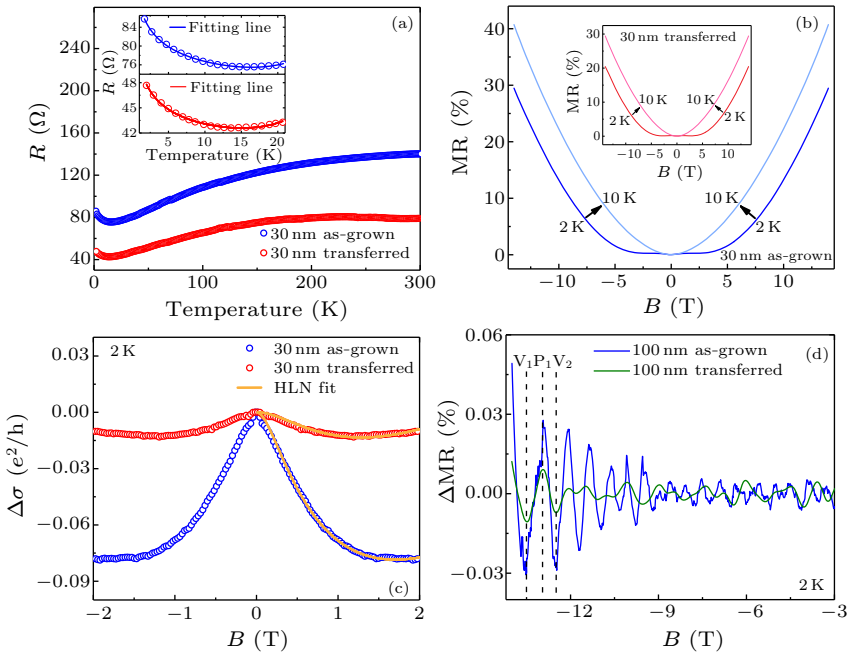

Fig. 4. Transport properties of transferred WTe_2 membranes. (a) R–T curves of the as-grown films and transferred membranes. Inset shows the enlarged low-temperature region and the corresponding fitting lines. (b) MR curves at 2 K and 10 K. (c) The fitted magnetoconductance curves, as converted from (b). (d) The distinct SdH oscillations of 100-nm as grown and transferred samples after a smooth subtraction of background from the MR curves (see the Supplementary Material).

In summary, we have demonstrated a reliable wet transfer methodology for preparing large-area, high-quality freestanding single-crystalline WTe_2 membranes. These membranes can be nondestructively transferred onto any foreign substrate. Moreover, WL/WAL characteristics and SdH quantum oscillations are maintained after transfer, indicating the feasibility and practicality of this methodology. The transferred freestanding single-crystalline WTe_2 membranes could easily be stacked to form artificial WTe_2 heterostructures, based on diverse functional substrates. Our findings not only offer the prospect of fabricating atomic-level Weyl freestanding membranes for atom manufacturing, but also advance the unrestricted integration of topological quantum materials for device applications.

References

[1] Soluyanov A A, Gresch D, Wang Z, Wu Q, Troyer M, Dai X and Bernevig B A 2015 *Nature* **527** 495
[2] Ali M N, Xiong J, Flynn S, Tao J, Gibson Q D, Schoop L M, Liang T, Haldolaarachchige N, Hirschberger M, Ong N P and Cava R J 2014 *Nature* **514** 205
[3] Jiang J, Tang F, Pan X C, Liu H M, Niu X H, Wang Y X, Xu D F, Yang H F, Xie B P, Song F Q, Dudin P, Kim T K, Hoesch M, Das P K, Vobornik I, Wan X G and Feng D L 2015 *Phys. Rev. Lett.* **115** 166601
[4] Kang D, Zhou Y, Yi W, Yang C, Guo J, Shi Y, Zhang S, Wang Z, Zhang C, Jiang S, Li A, Yang K, Wu Q, Zhang G, Sun L and Zhao Z 2015 *Nat. Commun.* **6** 7804
[5] Pan X C, Chen X, Liu H, Feng Y, Wei Z, Zhou Y, Chi Z,

Pi L, Yen F, Song F, Wan X, Yang Z, Wang B, Wang G and Zhang Y 2015 *Nat. Commun.* **6** 7805
[6] Tang S J, Zhang C F, Wong D, Pedramrazi Z, Tsai H, Jia C J, Moritz B, Claassen M, Ryu H, Kahn S, Jiang J, Yan H, Hashimoto M, Lu D H, Moore R G, Hwang C, Hwang C, Hussain Z, Chen Y L, Ugeda M M, Liu Z, Xie X M, Devereaux T P, Crommie M F, Mo S and Shen Z X 2017 *Nat. Phys.* **13** 683
[7] Wu S F, Fatemi V, Gibson Q D, Watanabe K J, Taniguchi T, Cava R J and Jarillo-Herrero P 2018 *Science* **359** 76
[8] Fei Z, Zhao W, Palomaki T A, Sun B, Miller M K, Zhao Z, Yan J, Xu X and Cobden D H 2018 *Nature* **560** 336
[9] Ma Q, Xu S Y, Shen H, MacNeill D, Fatemi V, Chang T R, Mier V A M, Wu S, Du Z, Hsu C H, Fang S, Gibson Q D, Watanabe K, Taniguchi T, Cava R J, Kaxiras E, Lu H Z, Lin H, Fu L, Gedik N and Jarillo-Herrero P 2019 *Nature* **565** 337
[10] Kang K, Li T, Sohn E, Shan J and Mak K F 2019 *Nat. Mater.* **18** 324
[11] Song S, Sim Y, Kim S Y, Kim J H, Oh I, Na W, Lee D H, Wang J, Yan S, Liu Y, Kwak J, Chen J H, Cheong H, Yoo J W, Lee Z and Kwon S Y 2020 *Nat. Electron.* **3** 207
[12] Wang A Q, Ye X G, Yu D P and Liao Z M 2020 *ACS Nano* **14** 3755
[13] Wang L M, Zou X M, Lin J, Jiang J Y, Liu Y, Liu X Q, Zhao X, Liu Y F, Ho J C and Liao L 2019 *ACS Nano* **13** 4804
[14] Guo Q X, Wu Y, Xu L X, Gong Y, Ou Y B, Liu Y, Li L L, Yan Y, Han G, Wang D W, Wang L H, Long S B, Zhang B W, Cao X, Yang S W, Wang X M, Huang Y Z, Liu T, Yu G H, He K and Teng J 2020 *Chin. Phys. Lett.* **37** 057301
[15] Gong Y, Guo J W, Li J H, Zhu K J, Liao M H, Liu X Z, Zhang Q H, Gu L, Tang L, Feng X, Zhang D, Li W, Song C L, Wang L L, Yu P, Chen X, Wang Y Y, Yao H, Duan W H, Xu Y, Zhang S C, Ma X C, Xue Q K and He K 2019 *Chin. Phys. Lett.* **36** 076801
[16] Yuan X, Cheng P H, Zhang L Q, Zhang C, Wang J Y, Liu Y W, Sun Q Q, Zhou P, Zhang D W, Hu Z G, Wan X G, Yan H G, Li Z Q and Xiu F X 2017 *Nano Lett.* **17** 2211
[17] Zhang M H, Wang X F, Song F Q and Zhang R 2018 *Chin. Phys. B* **27** 097307
[18] Zhang E, Chen R, Huang C, Yu J, Zhang K, Wang W, Liu S, Ling J, Wan X, Lu H Z and Xiu F X 2017 *Nano Lett.* **17** 878
[19] Zhou J, Liu F, Lin J, Huang X, Xia J, Zhang B, Zeng Q, Wang H, Zhu C, Niu L, Wang X, Fu W, Yu P, Chang T R, Hsu C H, Wu D, Jeng H T, Huang Y, Lin H, Shen Z, Yang C, Lu L, Suenaga K, Zhou W, Pantelides S T, Liu G and Liu Z 2017 *Adv. Mater.* **29** 1603471
[20] Fan S D, Vu Q A, Tran M D, Adhikari S and Lee Y H 2020 *2D Mater.* **7** 022005
[21] Hong S S, Gu M Q, Verma M, Harbola V, Wang B Y, Lu D, Vailionis A, Hikita Y, Pentcheva R, Rondinelli J M and Hwang H Y 2020 *Science* **368** 71
[22] Kum H S, Lee H, Kim S, Lindemann S, Kong W, Qiao K, Chen P, Irwin J, Lee J H, Xie S, Subramanian S, Shim J, Bae S H, Choi C, Ranno L, Seo S, Lee S, Bauer J, Li H, Lee K, Robinson J A, Ross C A, Schlom D G, Rzchowski M S, Eom C B and Kim J 2020 *Nature* **578** 75
[23] Yun S J, Chae S H, Kim H, C P J, Park J H, Han G H, Lee J S, Kim S M, M O H, Seok J, Jeong M S, Kim K K and Lee Y H 2015 *ACS Nano* **9** 5510
[24] Gao Y, Liu Z, Sun D M, Huang L, Ma L P, Yin L C, Ma T, Zhang Z, Ma X L, Peng L M, Cheng H M and Ren W 2015 *Nat. Commun.* **6** 8569
[25] Gao M, Zhang M H, Niu W, Chen Y Q, Gu M, Wang H Y, Song F Q, Wang P, Yan S C, Wang F Q, Wang X R, Wang X F, Xu Y B and Zhang R 2017 *Appl. Phys. Lett.* **111** 031906
[26] Chen Y Q, Chen Y D, Ning J A, Chen L M, Zhuang W Z, He L, Zhang R, Xu Y B and Wang X F 2020 *Chin. Phys. Lett.* **37** 017104
[27] Tu N H, Tanabe Y, Satake Y, Huynh K K, Le P H, Matsushita S Y and Tanigaki K 2017 *Nano Lett.* **17** 2354
[28] Kong W D, F W S, Richard P, Lian C S, T W J, Yang C L, Shi Y G and Ding H 2015 *Appl. Phys. Lett.* **106** 081906
[29] Cai P L, Hu J, He L P, Pan J, Hong X C, Zhang Z, Zhang J, Wei J, Mao Z Q and Li S Y 2015 *Phys. Rev. Lett.* **115** 057202
[30] Niu W, Gao M, Wang X F, Song F Q, Du J, Wang X R, Xu Y B and Zhang R 2016 *Sci. Rep.* **6** 26081
[31] Liao Z L, Li F M, Gao P, Li L, Guo J D, Pan X Q, Jin R, Plummer E W and Zhang J D 2015 *Phys. Rev. B* **92** 125123
[32] Ziese M 2003 *Phys. Rev. B* **68** 132411
[33] Xu Y, Zhang J C, Cao G X, Jing C and Cao S X 2006 *Phys. Rev. B* **73** 224410
[34] Knap W, Skierbiszewski C, Zduniak A, Litwin-Staszewska E and Bertho D 1996 *Phys. Rev. B* **53** 3912
[35] Zhang K, Pan H Y, Wei Z X, Zhang M H, Song F Q, Wang X F and Zhang R 2017 *Chin. Phys. B* **26** 096101
[36] Zhang M H, Li Y, Song F Q, Wang X F and Zhang R 2017 *Chin. Phys. B* **26** 127305
[37] Fatemi V, Gibson Q D, Watanabe K J, Taniguchi T, Cava R J and Jarillo-Herrero P 2017 *Phys. Rev. B* **95** 041410

Supplementary Material:

Large-Area Freestanding Weyl Semimetal WTe_2 Membranes

Yequan Chen(陈业全)[1], Ruxin Liu(刘汝新)[1], Yongda Chen(陈勇达)[1], Xiao Yuan(袁霄)[1], Jiai Ning(宁纪爱)[1], Chunchen Zhang(张纯臣)[2], Liming Chen(陈立明)[1], Peng Wang(王鹏)[2], Liang He(何亮)[1], Rong Zhang(张荣)[1], Yongbing Xu(徐永兵)[1*], and Xuefeng Wang(王学锋)[1*]

[1]Jiangsu Provincial Key Laboratory of Advanced Photonic and Electronic Materials, School of Electronic Science and Engineering, and Collaborative Innovation Center of Advanced Microstructures, Nanjing University, Nanjing 210093, China

[2]College of Engineering and Applied Sciences, Nanjing University, Nanjing 210093, China

Supported by the National Key R&D Program of China under Grant No. 2017YFA0206304, the National Natural Science Foundation of China under Grant Nos. 11874203, 61822403, U1732159, 11774160 and 61427812, and the Fundamental Research Funds for the Central Universities under Grant. No. 021014380080.

*Corresponding authors. Email: xfwang@nju.edu.cn; ybxu@nju.edu.cn

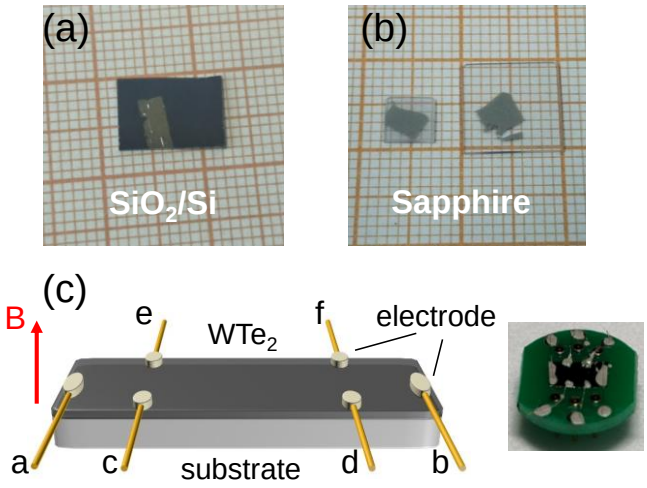

Fig. S1. Photographs of the transferred WTe_2 membranes on SiO_2/Si (a) and sapphire (b). (c) Diagrammatic sketch (left) and photograph (right) of WTe_2 samples for transport measurements. The standard six-probe method is employed, and the external magnetic field is vertical to the sample surface.

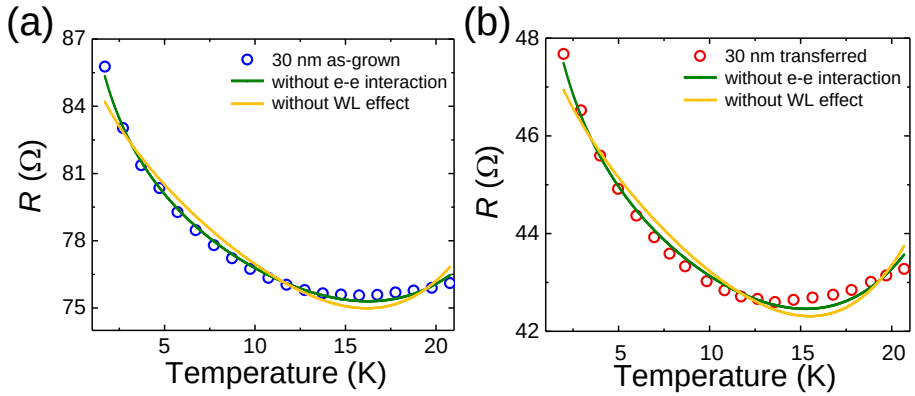

Fig. S2. (a) Low-temperature *R-T* curve of 30-nm as-grown WTe_2 films and corresponding fitting lines without e-e interaction (green) and without WL effect (yellow), respectively. (b) Low-temperature *R-T* curve of 30-nm transferred WTe_2 membrane and corresponding fitting lines without e-e interaction (green) and without WL effect (yellow), respectively.

Here, the quantum interference effect is used to explain this unusual increase in resistance below 15 K. Both e-e interaction and WL effect contribute to this phenomenon, based on equation (1) (which takes into account the localization theory and the insensitivity of e-e interaction).

The low-temperature *R-T* curve of the 30-nm WTe_2 membrane before and after transfer is fitted without e-e interaction (green) and without WL effect (yellow), as shown in (a) and (b), respectively. However, we cannot obtain a perfect fitting, as shown in the inset of Fig. 2(a).

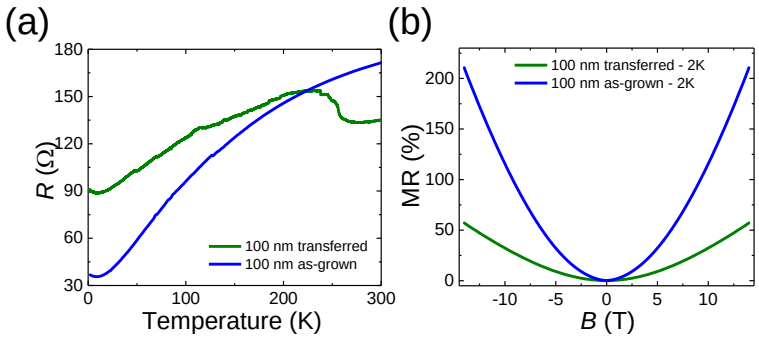

Fig. S3. (a) *R-T* curves and MR curves of 100-nm as-grown WTe_2 films and transferred membranes, respectively.

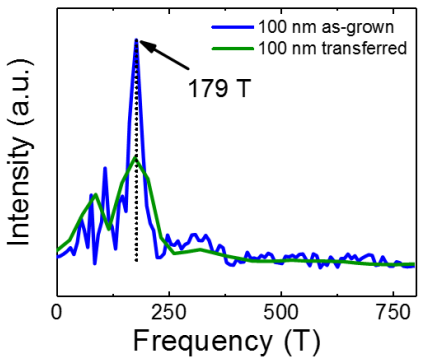

Fig. S4. FFT of the SdH quantum oscillations taken from Fig. 4(d).

By means of FFT, the frequency of the SdH quantum oscillations can be deduced as~179 T. Based on the Onsager relation, $F=(\hbar/2\pi e)A_F$, where $\hbar$ is the reduced Planck's constant and A_F is the cross-sectional area of this Fermi pocket normal to the field, A_F can be extracted to be 0.017Å^{-2}. Furthermore, the Fermi wave vector, k_F = 0.074Å^{-1}, can be extracted via a circular cross-sectional approximation.

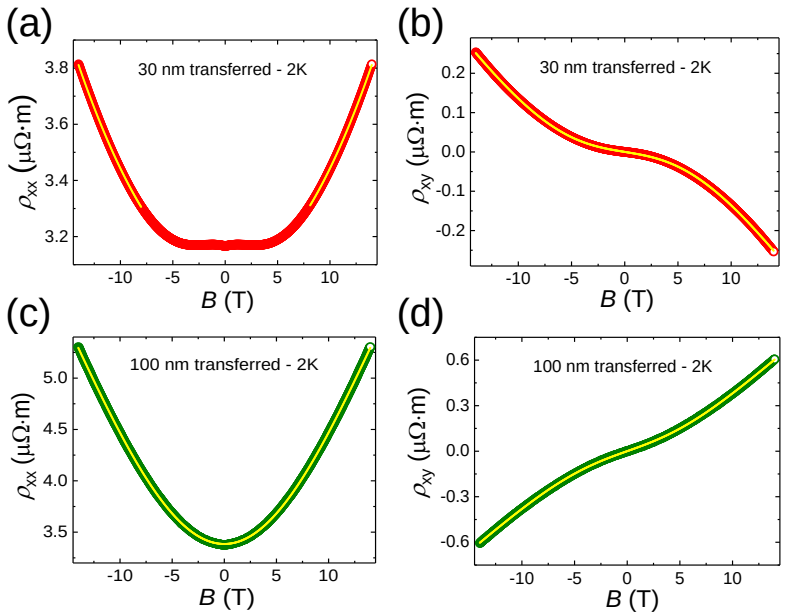

Fig. S5. Two-carrier model analysis. Field-dependent longitudinal resistivity, ρ_{xx}, and Hall resistivity, ρ_{xy}, of the 30-nm and 100-nm transferred membranes, respectively, at 2 K, fitted via the two-carrier model. The data in (a) between -8 T and 8 T are excluded from the fitting process due to the presence of distinct WL and WAL effects.

Here, the conventional two-carrier model is used to fit the field-dependent resistivity, ρ_{xx}, and Hall resistivity, ρ_{xy}, simultaneously:

$$\rho_{xx} = \frac{1}{e}\frac{(p\mu_h+n\mu_e)+(p\mu_h\mu_e^2+n\mu_e\mu_h^2)B^2}{(p\mu_h+n\mu_e)^2+(p-n)^2\mu_h^2\mu_e^2B^2},$$

$$\rho_{xy} = \frac{B}{e}\frac{(p\mu_h^2-n\mu_e^2)+(p-n)\mu_h^2\mu_e^2B^2}{(p\mu_h+n\mu_e)^2+(p-n)^2\mu_h^2\mu_e^2B^2},$$

where p and n represent the density of holes and electrons, and μ_h and μ_e denote the Hall mobility of holes and electrons, respectively.